A full-dimensional wave packet dynamics study of the photodetachment spectra of FCH 4−

Juliana Palma and Uwe Manthe

Additional information on J. Chem. Phys.
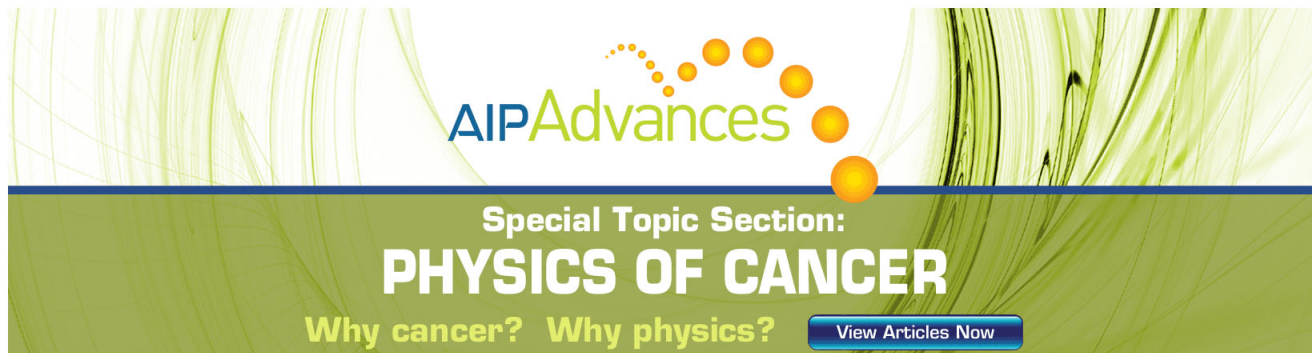
A full-dimensional wave packet dynamics study of the photodetachment spectra of FCH_4^-

Juliana Palma[1,a)] and Uwe Manthe[2,b)]

[1]*Departamento de Ciencia y Tecnología, Universidad Nacional de Quilmes, Sáenz Peña 352, Bernal B1876BXD, Argentina*
[2]*Theoretische Chemie, Fakultät für Chemie, Universität Bielefeld, Universitätsstr. 25, D-33615 Bielefeld, Germany*

The low-resolution photodetachment spectrum of FCH_4^- is studied in full dimensionality employing the multi-configurational time-dependent Hartree approach and potential energy surfaces recently developed by Bowman and co-workers. The computed spectrum qualitatively agrees with the low-resolution spectrum measured by Neumark and co-workers. It displays two peaks which can be assigned to different vibrational states of methane in the quasi-bound $F \cdot CH_4$ van der Waals complex. The first intense peak correlates to methane in its vibrational ground state while the second much smaller peak results from methane where one of the bending modes is excited. The present simulations consider only a single potential energy surface for the neutral FCH_4 system and thus do not include spectral contributions arising from transitions to excited electronic states correlating to the $F(^2P) + CH_4$ asymptote. Considering the quantitative differences between the computed and the experimental spectra, one cannot decide whether beside the vibrational excitation of the methane fragment also electronic excitation of FCH_4 contributes to the second peak in the experimental photodetachment spectrum. © *2012 American Institute of Physics*. [http://dx.doi.org/10.1063/1.4737382]

I. INTRODUCTION

The dynamics of a selected number of gas phase reactions has been characterized in great detail thanks to the effort of both, experimental and theoretical investigations. In that regard, the most prominent examples are $H + H_2 \rightarrow H_2 + H$ and $F + H_2 \rightarrow HF + H$.[1–13] Thus, while detailed experiments provided comprehensive information for these two reactions, accurate quantum computations allowed such information to be rationalized and understood. Other three- and tetra-atomic reactions have also been thoroughly investigated.[1–3,14,15] Altogether, these studies helped to unravel the details of many reactive collisions in the gas phase and to build up the basis of our current understanding of the subject. However, while the investigation of three- and four-atom reactions is still an ongoing process, a significant part of the attention has moved to the treatment of larger and more complex systems. In that connection, reactions of the type $X + CH_4 \rightarrow HX + CH_3$, with X=H, F, and Cl have become prototypes and are currently receiving a lot of attention.[16–62] Thus, while X=H is the preferred option for theoreticians,[48–61] X=F, Cl are the preferred ones for experimentalists.[16–47]

As the size of the reactive system increases its dynamics becomes richer and features that were not present in smaller systems appear. At the same time both, experimental and theoretical investigations, have to address new challenges to make their study possible. During the last ten years, advances in reactive scattering experiments have uncovered many details of the dynamics of the $F + CH_4 \rightarrow HF + CH_3$ reaction.[16–30] These advances have allowed, for example, to describe its mode-selected chemistry[26–28] and mode-specific dynamics[17,28] to a good extent. Moreover, it has been possible to determine the correlation between the final states of the co-products, shedding light about the way in which different modes of motion interact with each other and with the motion along the reaction path.[16,18–20,23–25,29] Finally, experiments that suggest the existence of reactive resonances,[21,22] similar to the ones found in the $F + H_2 \rightarrow HF + H$ reaction,[5,7,8,10,12,13,63] have also been reported. Unfortunately, advances from the theoretical side were not so fast and the information obtained from these experiments is still waiting for explanations founded on accurate quantum computations. There have been, nevertheless, many theoretical investigations of this reaction based on quasi-classical trajectories,[64–75] transition-state theory,[76,77] and reduced dimensionality computations.[78,79]

The $F + CH_4 \rightarrow HF + CH_3$ reaction has also been studied using photodetachment spectroscopy, a technique employed to get direct access to the transition state of reactive systems.[80–82] Photodetachment experiments have provided detailed information on the dynamics of several reactions and played a central role in the study of $F + H_2 \rightarrow HF + H$.[83–86] Interestingly, in that case, the differences between experimental and theoretical results helped to highlight the limitations of both, calculations and experiments, promoting the quest for improvements on the two sides. Last year the low-resolution photodetachment spectra of several XCH_4^- anions including FCH_4^- were presented and their most salient

a)E-mail: juliana@unq.edu.ar.
b)E-mail: uwe.manthe@uni-bielefeld.de.

features were interpreted with the assistance of *ab-initio* calculations.[87] More recently, high-resolution spectra for FCH_4^- and FCD_4^-, which show a very rich fine structure, were obtained by Neumark and co-workers.[86] A dynamical interpretation of the results of these experiments has not be given yet.

So far, the only theoretical approach that has provided full-dimensional quantum computations for six-atom reactions is the multi-configurational time-dependent Hartree (MCTDH) method.[88,89] The first of such studies appeared nearly twelve years ago. It consisted of the evaluation of the thermal rate constants for the $H + CH_4 \rightarrow H_2 + CH_3$ reaction.[51,90,91] Shortly after, similar computations were also performed for $O(^3P) + CH_4 \rightarrow OH + CH_3$.[92] What made such calculations possible, in spite of the more limited computational resources of that time, was the combination of the MCTDH approach, for the efficient propagation of the wave packets, with the formalism of the flux-flux correlation function, for the direct computation of k(T). Over the years, other k(T) calculations appeared for the $H + CH_4 \rightarrow H_2 + CH_3$ reaction using different PESs (Refs. 54 and 93–95) and coordinate systems[96] as well as studying isotopic substituions.[55,56] More recently, an approach to compute the initial state-selected (J = 0) reaction probabilities based on the evaluation of the thermal flux eigenfunctions[97–99] was successfully applied to this reaction.[58,59]

We are now extending the range of polyatomic bimolecular reactions studied with the MCTDH method, by presenting the first accurate computations for the $F + CH_4 \rightarrow HF + CH_3$ system. But, instead of calculating reaction attributes such as rate constants, or reaction probabilities, we characterize the dynamics at the entrance channel and the transition-state region through the simulation of the photodetachment spectra of FCH_4^-. The results of the computations are compared with recent experiments and the differences between them are thoroughly discussed. Moreover, a dynamical interpretation of the main features of the spectrum is presented. From a theoretical point of view, this is a very challenging system, not only because of its high dimensionality, but also because of the topology of its potential energy surface. The calculations presented in this article were obtained with the analytical surfaces developed by Czakó *et al.* for both, the anion[100] and the electronic ground[65] state of the neutral species. Contributions from excited electronic states were not taken into account.

The rest of the article is organized as follows. In Sec. II we describe the procedure employed to perform the calculations. We present there the coordinate system and its corresponding Hamiltonian, discuss some characteristics of the potential energy surface, underline the theory used to calculate the photodetachment spectra, and present the basis sets employed at the different stages of the MCTDH computation. The results of the calculations are presented in Sec. III. There we show the dynamics of the evolving wave packet on the neutral surface, present the outcome of different convergence tests for the computed spectrum, compare the computed spectra with the experimental ones, and discuss the results. Section IV closes the article presenting the conclusions of this work.

II. SYSTEM DESCRIPTION

A. Coordinates and kinetic energy operator

The present work uses an analogous coordinate system as recent MCTDH-based studies of the $H + CH_4 \rightarrow H_2 + CH_3$ reaction.[58,59,96] Therefore, only a brief discussion will be presented here.

The methyl group is described by the curvilinear system introduced in Ref. 101. It is based on a $3 + 1$ Radau construction. Three vectors, $\mathbf{r}_1$, $\mathbf{r}_2$, and $\mathbf{r}_3$, connect the Radau point with the hydrogen atoms of the CH_3 group. A coordinate frame is attached to this fragment so that its z axis is aligned to the trisector of the Radau vectors, while the plane containing the trisector and one of the hydrogen atoms is defined as the xz plane. Three angles, θ, χ, and ϕ, define the orientation of the Radau vectors in this body-fixed frame. The umbrella vibration is described by θ, which measures the angle between each of the Radau vectors and the z axis. The other two angles describe the symmetry-breaking bending vibrations of the group (see Ref. 101 for more details and a pictorial description). The lengths of the Radau vectors are expressed in terms of the polar coordinates ρ, ϑ_ρ, and ϕ_ρ as

$$\begin{aligned} r_1 &= \rho \sin(\vartheta_\rho) \cos(\phi_\rho), \\ r_2 &= \rho \sin(\vartheta_\rho) \sin(\phi_\rho), \\ r_3 &= \rho \cos(\vartheta_\rho). \end{aligned} \quad (1)$$

Therefore, ρ essentially describes the symmetric stretching vibration of the group while ϑ_ρ and ϕ_ρ account for the symmetry-breaking stretching vibrations.

The positions of the remaining hydrogen atom and the fluorine atom, are given by Jacobi vectors which are appropriate to describe the reactant channel of the $F + CH_4 \rightarrow HF + CH_3$ reaction. Thus, $\mathbf{r}$ goes from the center of mass of the CH_3 group to the remaining H atom, while $\mathbf{R}$ goes from the center of mass of methane to the F atom. Both vectors, $\mathbf{r}$ and $\mathbf{R}$, were expressed in stereographic coordinates[96] (r, s, t) and (R, S, T), respectively. Here, r and R stand for the lengths of the vectors while (s, t) and (S, T) are their stereographic projections. These projections can be calculated from the usual polar angles as

$$\begin{aligned} s &= \tan(\vartheta_r/2) \cos(\phi_r), & S &= \tan(\vartheta_R/2) \cos(\phi_R), \\ t &= \tan(\vartheta_r/2) \sin(\phi_r), & T &= \tan(\vartheta_R/2) \sin(\phi_R). \end{aligned} \quad (2)$$

Using the coordinates described above the kinetic energy operator takes the form

$$\hat{T} = \hat{T}_{CH_3} + \hat{T}_{H_R} + \hat{T}_{H_r}. \quad (3)$$

Here, $\hat{T}_{H_R}$ and $\hat{T}_{H_r}$ are the kinetic energy operators for the Jacobi vectors $\mathbf{r}$ and $\mathbf{R}$, respectively,

$$\hat{T}_{H_R} = -\frac{1}{2\mu_R} \frac{\partial^2}{\partial R^2} + \frac{1}{2\mu_R R^2} \hat{\mathbf{J}}_{\mathbf{R}}^2, \quad (4)$$

$$\hat{T}_{H_r} = -\frac{1}{2\mu_r} \frac{\partial^2}{\partial r^2} + \frac{1}{2\mu_r r^2} \hat{\mathbf{J}}_{\mathbf{r}}^2, \quad (5)$$
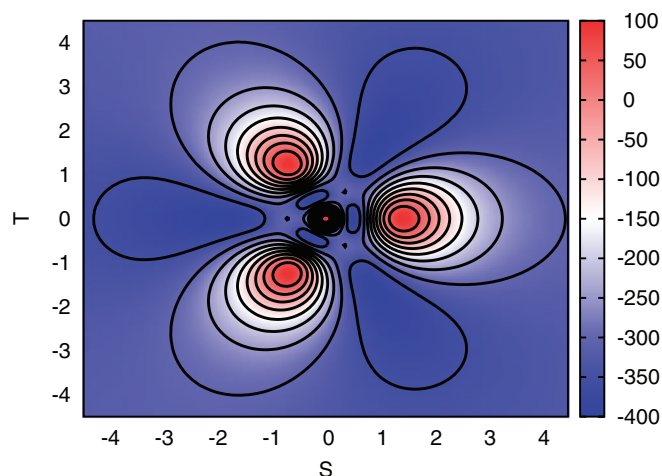
FIG. 1. Contour plot of the neutral PES for $R = 2.97$ Å. Contour levels are plot every 50 cm^{-1} starting at -350 cm^{-1}.

FIG. 2. Contour plot of the neutral PES for $S = 0$. The black dot indicates the Frank-Condon point. Contour levels are plot every 40 cm^{-1} starting at -380 cm^{-1}.

where μ_R and μ_r are the corresponding reduced masses. Please note that, throughout the article, we use atomic units so that $\hbar = 1$. The angular momentum operators $\hat{\mathbf{J}}_{\mathbf{R}}$ and $\hat{\mathbf{J}}_{\mathbf{r}}$ depend on the coordinates (S, T) and (s, t), respectively, and are explicitly given in Ref. 96. The kinetic energy operator $\hat{T}_{CH_3}$, which accounts for the internal motion of the CH$_3$ group and its relative motion to the Jacobi vectors, is based on the mean-field C$_{3v}$ kinetic energy operator derived in Ref. 101. The specific form valid for the present system is taken from Ref. 96.

B. Potential energy surfaces

The potential energy surfaces employed in this work for the anion and the neutral species were developed by Czakó *et al.*, who also described their main features in Refs. 100 and 65, respectively. In this section we will discuss some characteristics of the neutral surface, mainly in connection with the coordinates that depict the movement of the F atom with respect to the methane molecule. Figure 1 shows a contour plot of the PES as a function of coordinates S and T. It was calculated by fixing R to its Frank-Condon value and relaxing all other coordinates. Similarly, Fig. 2 shows a contour plot of the PES as a function of coordinates R and T. This plot was obtained by fixing S to its Frank-Condon value while relaxing the remaining coordinates.

Figure 1 clearly shows the symmetries of the system. To fully understand the picture it is important to note that the stereographic coordinates map all the points that are on the northern hemisphere inside the unit circle while everything that is in the southern hemisphere is mapped from the unit circle to the infinite. In our coordinate system the z axis is aligned with the trisector of the C–H bonds of CH$_3$. Since at equilibrium CH$_4$F$^-$ has C$_{3v}$ symmetry, the F atom is also on the z axis and therefore both coordinates, S and T, are equal to zero (see Eq. (2)). Accordingly, the equilibrium configuration of the anion surface corresponds to the central point of Fig. 1, which is a local maximum. The other three maxima of the figure correspond to configurations in which the F atom is
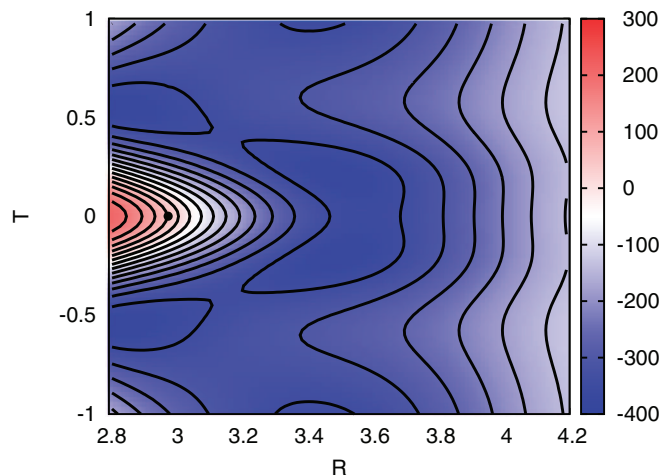
aligned to the remaining H atoms. The coordinates (S, T) for such points are $(1.41, 0.0)$, $(-0.71, 1.23)$, and $(-0.71, -1.23)$. It should be noted that these H atoms are located in the southern hemisphere. Therefore, their stereographic coordinates lie all outside the unity circle. Since the stereographic projections do not preserve areas and distances (i.e., they are not isomorphic), the contour lines around those maxima enclose larger areas than the one corresponding to the H atom located at the north pole.

One can now draw imaginary lines connecting the maximum at the center of the figure with the other three maxima. These lines would contain the values of S and T corresponding to the edges of the tetrahedron that connect the H atom at the north pole with the remaining H atoms. Looking at Fig. 1, one can now see that there is a minimum centered on each of those edges. Three more symmetry-equivalent minima, corresponding to the edges that connect the H atoms in the southern hemisphere between each other, can also be seen in the figure. Once again, because of the lack of isomorphism of the stereographic coordinates these minima occupy larger areas than the ones connecting with the H atom in the north pole.

Three tiny relative maxima appear in Fig. 1 in between the minima located at the edges of the tetrahedron. Such maxima correspond to configurations in which the F atom is aligned to the center of the faces. There is a fourth of such maximum which does not appear in the figure because it is just at the south pole, the only point of the sphere for which there is not stereographic projection. In general, the nature and the relative importance of the different wells and bumps in figures such as Fig. 1 depend on the value at which R is fixed. This can be better seen in Fig. 2 where the significance of the van der Waals wells located at larger values of R is readily appreciated. The black dot at $R = 2.97$ Å, $T = 0.0$ indicates the position of the Frank-Condon point. The figure shows that, in the R direction, the potential decreases relatively rapidly between the Frank-Condon point and $R \approx 3.30$ Å. Then, it starts to increase again from $R \approx 3.75$ Å. In between, the potential has a broad and rather flat minimum. At the Frank-Condon point the potential also decreases in the T direction for both,

positive and negative values of T, until it reaches the minima located at $T \approx \pm 0.55$ (note the symmetry about $T = 0$). These minima are connected to the ones situated at larger values of R through very small barriers. Therefore, there is nearly no restrictions for changing the relative orientation between the F atom and the methane. Besides, since the depths of the different minima are similar, there is not a single, clearly preferred orientation.

We found that the most stable van der Waals complexes are the ones in which the F atom is placed in front of the edges of the tetrahedron. The equilibrium configuration for these complexes are located at $R = 2.94$ Å and have an energy of 388 cm^{-1} below the F + CH$_4$ asymptote. Notably, minima with this configuration have not been described for the *ab initio* results. Instead, it has been reported that the *ab initio* calculations show two types of van der Waals complexes in the reactant channel, both of them with C$_{3v}$ symmetry.[65] In the deepest minima, $E = -158$ cm^{-1}, the F atom is aligned to the center of the faces of the tetrahedron (F–C–H configuration) while in the other, $E = -40$ cm^{-1}, the F atom is aligned to the vertex (F–H–C configuration). On top of these differences between analytical and *ab initio* potential energy surfaces one should keep in mind that, as described in Ref. 65, the equilibrium parameters of the *ab initio* PES have themselves large uncertainties because of the extremely high level of theory required to accurately describe this part of the surface. In this context the calculation of the photodetachment spectrum using accurate quantum dynamical methods acquires particular importance since the comparison between accurate computations and experiments can be used to identify those features of the PES that need to be improved.

C. Photodetachment spectra

The evaluation of the spectrum is based on the assumption that the only state of the anion to be considered is the vibrational ground state with J = 0. Additionally, it is assumed that the transition dipole matrix element associated with the electronic transition between the anion and the neutral species does not depend on the nuclear coordinates nor on the energy of the ejected electron. Under these premises the photodetachment spectrum can be calculated as

$$\sigma(E) = C \, Re \left[\int_0^\infty dt \, e^{iEt} S(t) \right], \tag{6}$$

where C is a constant that incorporates the value of the transition dipole matrix element. $S(t)$ is the autocorrelation function of the initial wave packet

$$S(t) = \langle \Psi(0) | \Psi(t) \rangle = \langle \Psi(0) | e^{-i(\hat{H}_n - E_i)t} \, \Psi(0) \rangle. \tag{7}$$

Here the initial wavefunction $\Psi(0)$ is the wavefunction of the vibrational ground state of the anion, $\hat{H}_n$ is the Hamiltonian operator corresponding to the neutral CH$_4$F complex, and E_i is the ground state energy of the anion. Since the zero of energy for the computations on the neutral surface was set at the potential energy minimum of the asymptotic F + CH$_4$ channel, we have

$$E_i = -(E_a + D_e) + ZPE(CH_4F^-). \tag{8}$$

TABLE I. Parameters for the absorbing potentials in atomic units.

V_r	0.18	V_ρ	0.18
r_0	3.37	ρ_0	180.0
r_{max}	4.34	ρ_{max}	220.0

The values employed for the electron affinity of the F atom and the dissociation energy of the complex were $E_a = 3.401$ eV = 27431.5 cm^{-1} and $D_e = 2398$ cm^{-1}.[100] On the other hand, the values employed for the zero point energy of the anion complex, ZPE(CH$_4$F$^-$), depend on the basis set used in the computations and are presented below, where the characteristics of these basis sets are discussed. It should be noted that the energy E appearing in Eq. (6) is equivalent to the electron binding energy (eBE) usually employed to present the results of electron detachment experiments.

Absorbing potentials were added to $\hat{H}_n$ to remove the fraction of the evolving wave packet that goes into the HF + CH$_3$ channel. Two absorbing potentials $\epsilon_r(r)$ and $\epsilon_\rho(\rho)$ depending on the coordinates r and ρ, respectively, were applied

$$\epsilon_r(r) = V_r \left(\frac{r - r_0}{r_{max} - r_0} \right)^4,$$

$$\epsilon_\rho(\rho) = V_\rho \left(\frac{\rho - \rho_0}{\rho_{max} - \rho_0} \right)^4. \tag{9}$$

The values employed for the parameters appearing in Eq. (9) are presented in Table I. Furthermore, since the initial wavefunction is real, the autocorrelation function at time t was obtained from the wavefunction at time $t/2$ as

$$S(t) = \langle e^{i(\hat{H}_n t/2 - E_i)} \Psi(0) | e^{-i(\hat{H}_n t/2 - E_i)} \Psi(0) \rangle$$

$$= \langle \Psi(t/2)^* | \Psi(t/2) \rangle. \tag{10}$$

In order to analyse the results of the dynamical simulations, the evolving wave packet can be decomposed into contributions corresponding to different vibrational states of methane. To see how this decomposition is done it is convenient to write the wave packet in a way that differentiates the parts that depend on the methane coordinates from the parts that depend on the fluorine coordinates. Introducing a collective coordinate $\mathbf{Q} = (r, s, t, \rho, \vartheta_\rho, \phi_\rho, \theta, \chi, \phi)$, which includes the nine coordinates describing the motions within the methane molecule and a collective coordinate $\mathbf{X} = (R, S, T)$ describing the motion of the F atom relative to the CH$_4$, the wavefunction can be written as

$$\Psi(\mathbf{X}, \mathbf{Q}, t) = \sum_N \psi_N(\mathbf{X}, t) \Phi_N(\mathbf{Q}), \tag{11}$$

where the $\Phi_N(\mathbf{Q})$ denote a complete (time-independent) basis of the nine-dimensional Hilbert space corresponding to the $\mathbf{Q}$ coordinates. As will be seen below, a transformation to this type of wavefunction representation can be efficiently achieved within the MCTDH framework. Defining (time-independent) projection operators $\hat{P}_N$ projecting onto $\Phi_N(\mathbf{Q})$ states,

$$\hat{P}_N = |\Phi_N\rangle\langle\Phi_N|, \tag{12}$$

the time-dependent populations of the $\Phi_N(\mathbf{Q})$ states,

$$P_N(t) = \langle \Psi(t)|\hat{P}_N|\Psi(t)\rangle = \langle \psi_N(t)|\psi_N(t)\rangle, \quad (13)$$

and the contributions $\sigma_N^{(0)}$ of the $\Phi_N(\mathbf{Q})$ states to the photodetachment spectra,

$$\sigma_N^{(0)}(E) = C\,Re\left[\int_0^\infty dt\, e^{iEt}\, S_N^{(0)}(t)\right],$$

$$S_N^{(0)}(t) = \langle \Psi(0)|\hat{P}_N|\Psi(t)\rangle = \langle \psi_N(0)|\psi_N(t)\rangle, \quad (14)$$

can be introduced.

If one identifies the $\Phi_N(\mathbf{Q})$ states in Eq. (11) with the vibrational eigenstates of methane, one can analyse the population dynamics in the methane fragment and the contribution of these states to the photodetachment spectrum. However, one should note that methane can dissociate in course of the dynamical process under consideration. Thus, the bound states of methane do not form a complete basis. Furthermore, the contributions $\sigma_N^{(0)}$ defined in Eq. (14) are not identical with the partial photodetachment spectra relating to the product state distribution. The partial photodetachment spectra $\sigma_N^{(\infty)}$, corresponding to the fraction of the spectra resulting in the methane fragment produced in the asymptotic vibrational state $\Phi_N(\mathbf{Q})$, would be given by

$$\sigma_N^{(\infty)}(E) = C\,Re\left[\int_0^\infty dt\, e^{iEt}\, S_N^{(\infty)}(t)\right],$$

$$S_N^{(\infty)}(t) = \langle \Psi(0)|\lim_{t'\to\infty} e^{i\hat{H}_n t'}\hat{P}_N e^{-i\hat{H}_n t'}|\Psi(t)\rangle. \quad (15)$$

The contributions $\sigma_N^{(0)}$ considered in the present work and the partial photodetachment spectra $\sigma_N^{(\infty)}$ would only be identical if the motion in the internal coordinates of the methane fragment $\mathbf{Q}$ and the other coordinates $\mathbf{X} = (R, S, T)$ were separable, i.e., if $[\hat{H}_n, \hat{P}_N] = 0$. This clearly is not a rigorously correct assumption for the present system. It would be completely inadequate for describing the dynamics of the $HF + CH_3$ channel. However, the Franck-Condon point of the CH_4F^- electron detachment is located towards the $F + CH_4$ channel, where the decoupling of the internal motion of methane from its relative motion with respect to the fluorine atom is a useful zero order approximation for the description of the van der Waals complexes. Thus, the calculation of the contributions $\sigma_N^{(0)}$ and the populations P_N has been introduced as an interpretational tool to analyse the dynamics of the CH_4F^- photodetachment process. On the other hand, we emphasize that the partial photodetachment spectra $\sigma_N^{(\infty)}$ of Eq. (15) have not been computed.

D. Wave packet propagation

The calculation of the photodetachment spectrum requires propagation in real and imaginary time. The initial wave packet, $\Psi(0)$, is generated by propagation in imaginary time on the PES of the CH_4F^- anion until convergence. Then this wavefunction is propagated in real time on the PES of the neutral CH_4F to obtain $\Psi(t)$. These imaginary and real time propagations are performed using the MCTDH approach.[88, 89] Thus, the multi-dimensional wavefunction $\Psi(x_1, x_2, \ldots, x_f, t)$

is represented as

$$\Psi(x_1, \ldots, x_f, t) = \sum_{j_1=1}^{n_1}\cdots\sum_{j_f=1}^{n_f} A_{j_1\cdots j_f}(t)\prod_{\kappa=1}^{f}\varphi_{j_\kappa}^{(\kappa)}(x_\kappa, t),$$

$$(16)$$

where the $\varphi_{j_\kappa}^{(\kappa)}(x_\kappa, t)$ are time-dependent basis functions, called single-particle functions (SPF), and the $A_{j_1\cdots j_f}$ are the corresponding expansion coefficients. The single-particle functions itself are represented employing time-independent basis sets $\{\chi_{i_\kappa}^{(\kappa)}(x_\kappa), i_\kappa = 1, 2, \ldots, N_\kappa\}$ in the respective co-ordinate (typically provided by a discrete variable representation (DVR) (Refs. 102–104) or fast Fourier transform (FFT) scheme[105])

$$\varphi_{j_\kappa}^{(\kappa)}(x_\kappa, t) = \sum_{i_\kappa=1}^{N_\kappa} c_{j_\kappa, i_\kappa}^{(\kappa)}(t)\chi_{i_\kappa}^{(\kappa)}(x_\kappa). \quad (17)$$

Equations of motion can be straightforwardly derived using the Dirac-Frenkel variational principle.[88, 89] The present work employs the correlation DVR approach[106] to evaluate the potential matrix elements appearing in the equations of motion and a constant mean-field integration (CMF) (Ref. 107) scheme, the CMF2 scheme of Ref. 108, to perform the time integration.

The SPF basis set sizes, n_κ, and the sizes of the time independent grids, N_κ, employed in the imaginary time and real time computations differ significantly. For the anion, only small amplitude vibrations in a single potential well were considered (see Ref. 109 for a more detailed discussion of the localisation of the CH_4F^- complex). Therefore, the computations are less demanding. Two different basis, presented in Table II, were employed to obtain the vibrational ground state. Basis set A_0 is appropriate for the basis sets A_1 and A_2 of the real time propagation while basis set B_0 is appropriate for basis set B_1 of the real time propagation. The zero point energies obtained with basis sets A_0 and B_0 are 9855.3 cm^{-1} and 9794.3 cm^{-1}, respectively. The last (more accurate) value is quite close to the accurate results of 9786.6 cm^{-1} and 9794.7 cm^{-1} reported by Wodraszka $et\ al.$[109] and Czakó $et\ al.$,[100] respectively. (It should be noted that errors of a few cm^{-1} can result from the approximations in the C_{3v} mean-field kinetic energy operator used to describe the methyl fragment.[96])

TABLE II. Basis sets employed in the imaginary time propagations. R and r are given in atomic units.

Coordinate	Primitive	N_κ	$n_\kappa(A_0)$	$n_\kappa(B_0)$
r	FFT [1.21:3.62]	32	3	3
s, t	FFT [−0.5:0.5]	32	4	4
R	FFT [2.77:8.08]	128	3	3
S, T	FFT [−1.0:1.0]	32	4	4
ρ	DVR	16	1	2
ϑ_ρ	DVR	16	1	2
φ_ρ	DVR	16	1	2
θ	DVR	32	3	3
ϕ	DVR	16	1	2
χ	DVR	16	1	2

TABLE III. Basis set A_1 for the real time propagation. R and r are given in atomic units.

Coordinate	Primitive	N_k	n_κ ($0 < t < 25$ fs)	n_κ ($t > 25$ fs)
r	FFT [1.21:5.06]	80	7	8
s, t	FFT [−0.5:0.5]	32	5	6
R	FFT [2.77:15.8]	440	7	8
S, T	FFT [−3.0:3.0]	180	6	7
ρ	DVR	16	1	1
ϑ_ρ	DVR	16	1	1
φ_ρ	DVR	16	1	1
θ	DVR	32	4	4
ϕ	DVR	16	1	1
χ	DVR	16	1	1

Significantly larger SPF basis sets and grid sizes are required for the neutral complex which shows large amplitude as well as dissociative motion. Furthermore, it was found that as the wave packet spreads out and moves towards the dissociative channels, some coordinates require more SPFs for an appropriate description. Therefore, to minimize the numerical effort, the sizes of the SPF basis sets were increased at some points in time. Calculations with various basis sets were performed and the three different basis sets presented in Tables III–V were found to be the most useful. They provide the most accurate results and allow one to systematically investigate the convergence achieved.

In order to analyze the results of the simulations, the evolving wave packet was decomposed into contributions corresponding to different vibrational states of methane (see Eqs. (11)–(14)). The vibrational eigenstates of methane were calculated employing block relaxation within the state-averaged MCTDH approach.[110] The 25 lowest vibrational states were computed considering the nine coordinates r, s, t, ρ, ϑ_ρ, ϕ_ρ, θ, χ, ϕ. The wavefunction representation used in this calculation is given in Table VI. Denoting the 25 wave packets Φ_N considered in these nine-dimensional state-averaged MCTDH calculations as

$$\Phi_N(x_1, \ldots, x_9) = \sum_{j_1=1}^{\tilde{n}_1} \cdots \sum_{j_9=1}^{\tilde{n}_9} \tilde{A}_{j_1 \cdots j_9, N} \prod_{\kappa=1}^{9} \tilde{\varphi}_{j_\kappa}^{(\kappa)}(x_\kappa) \quad (18)$$

(where the coordinates x_1 to x_9 represent r, s, t, ρ, ϑ_ρ, ϕ_ρ, θ, χ, ϕ) and the full 12D MCTDH wavefunction as

$$\Psi(x_1, \ldots, x_{12}, t) = \sum_{j_1=1}^{n_1} \cdots \sum_{j_{12}=1}^{n_{12}} A_{j_1 \cdots j_{12}}(t) \prod_{\kappa=1}^{12} \varphi_{j_\kappa}^{(\kappa)}(x_\kappa) \quad (19)$$

(where the coordinates x_{10}, x_{11}, x_{12} represent R, S, T), the functions $\psi_N(\mathbf{X}, t) = \psi_N(x_{10}, x_{11}, x_{12}, t)$ appearing in Eq. (11) can be straightforwardly obtained as

$$\psi_N(x_{10}, x_{11}, x_{12}, t) = \sum_{j_{10}=1}^{n_{10}} \cdots \sum_{j_{12}=1}^{n_{12}} B_{j_{10} j_{11} j_{12}, N} \prod_{\kappa=10}^{12} \varphi_{j_\kappa}^{(\kappa)}(x_\kappa)$$

$$(20)$$

with

$$B_{j_{10} j_{11} j_{12}, N}(t) = \sum_{j_1=1}^{\tilde{n}_1} \cdots \sum_{j_9=1}^{\tilde{n}_9} \tilde{A}_{j_1 \cdots j_9, N}^* \cdot \left(\sum_{l_9=1}^{n_9} \cdots \left(\sum_{l_2=1}^{n_2} \langle \tilde{\varphi}_{j_2}^{(2)} | \varphi_{l_2}^{(2)} \rangle \left(\sum_{l_1=1}^{n_1} \langle \tilde{\varphi}_{j_1}^{(1)} | \varphi_{l_1}^{(1)} \rangle A_{l_1 \cdots l_9 j_{10} j_{11} j_{12}}(t) \right) \right) \right). \quad (21)$$

III. RESULTS AND DISCUSSION

A. Dynamics of the wave packet

Two dimensional plots of the wave packet for different times as a function of coordinates (R, T) and (S, T) are presented in Figs. 3 and 4, respectively. The 2D probability density displayed there were obtained by integrating the 12D probability density $|\Psi(x_1, .., x_{12}, t)|^2$ over the remaining ten coordinates. In both cases, upper panel corresponds to $t = 0$, middle panel to $t = 50$ fs, and lower panel to $t = 100$ fs.

In Fig. 3, the line at $R = 2.63$ Å indicates the R value of the transition state for the $F + CH_4 \rightarrow HF + CH_3$ reaction. It can be readily noted that, as time passes, a small part of the

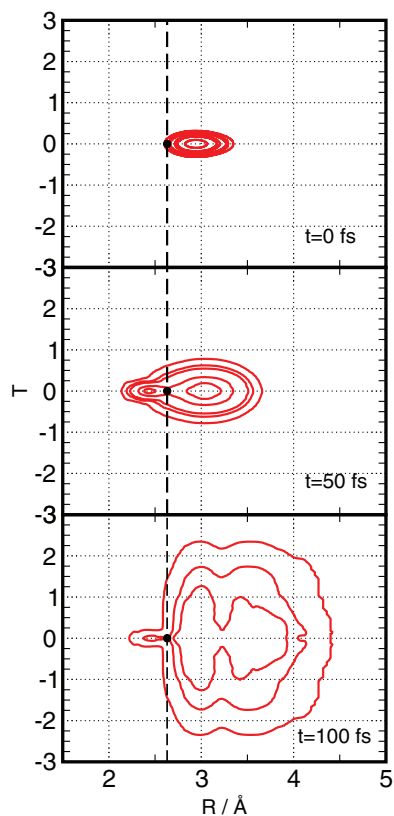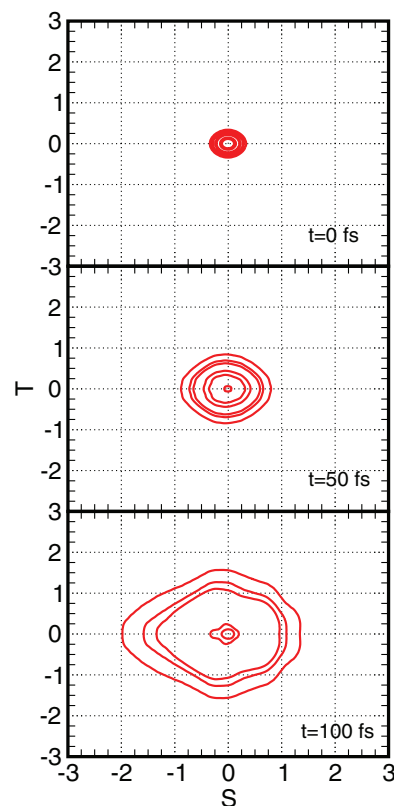TABLE IV. Basis set A_2 for the real time propagation. R and r are given in atomic units.

Coordinate	Primitive	N_k	n_κ ($0 < t \leq 25$ fs)	n_κ (25 fs $< t \leq 39$ fs)	n_κ ($t > 39$ fs)
r	FFT [1.21:5.06]	80	8	9	10
s, t	FFT [−0.6:0.6]	40	6	7	8
R	FFT [2.77:19.8]	580	8	9	10
S, T	FFT [−3.5:3.5]	210	7	8	9
ρ	DVR	16	1	1	1
ϑ_ρ	DVR	16	1	1	1
φ_ρ	DVR	16	1	1	1
θ	DVR	32	5	5	5
ϕ	DVR	16	1	1	1
χ	DVR	16	1	1	1

TABLE V. Basis set B_1 for the real time propagation. R and r are given in atomic units.

Coordinate	Primitive	N_k	n_κ ($0 < t < 25$ fs)	n_κ ($t > 25$ fs)
r	FFT [1.21:5.06]	80	7	8
s, t	FFT -0.5:0.5]	40	5	6
R	FFT [2.77:19.8]	580	7	8
S, T	FFT [-3.5:3.5]	210	6	7
ρ	DVR	210	2	2
ϑ_ρ	DVR	32	2	2
φ_ρ	DVR	32	2	2
θ	DVR	32	4	4
ϕ	DVR	16	2	2
χ	DVR	16	2	2

TABLE VI. Basis set employed in the computation of the first 25 vibrational states of CH_4. r is given in atomic units.

Coordinate	Primitive	N_k	n_κ
r	FFT [1.21:5.06]	64	4
s, t	FFT [-0.5:0.5]	32	5
ρ	DVR	16	4
ϑ_ρ	DVR	16	4
φ_ρ	DVR	16	4
θ	DVR	32	5
ϕ	DVR	16	5
χ	DVR	16	5

FIG. 4. Evolution of the wave packet in coordinates S and T. Contour levels are set at 1.0×10^{-5}; 5.0×10^{-5}; 1.0×10^{-4}; 5.0×10^{-4}; 1.0×10^{-3}, and 5.0×10^{-3}.

FIG. 3. Evolution of the wave packet in coordinates R and T. Contour levels are set at 1.0×10^{-5}; 5.0×10^{-5}; 1.0×10^{-4}; 5.0×10^{-4}; 1.0×10^{-3}; and 5.0×10^{-3}. The dashed line indicates the value of R at the TS.

wave packet moves towards the products side of the surface. As explained in Sec. II C, this part is absorbed since it does not contribute to the autocorrelation function. Consequently, there is a lost of the norm. This becomes first noticeable at about 5 fs. At $t = 100$ fs, 11% of the wave packet has been absorbed. At the longest time studied by any of our calculations, $t = 140$ fs, that number increases to 13%. The remaining part of the wave packet slowly moves to larger values of R. After 100 fs, the majority of the wave packet located on the reactant side of the surface has moved to the region of the outer van der Waals wells ($R > 3.30$ Å) (see Fig. 2 for the corresponding PES).

Besides, as the wave packet moves towards larger values of R, it also spreads in coordinates S and T (see Fig. 4). The initial collinear configuration is not favoured on the neutral surface. Therefore, the wave packet moves towards the surrounding minima which are symmetrically distributed around the Frank-Condon point. From there it then moves towards the van der Waals wells located at larger values of R. In the last panel of Fig. 4, corresponding to $t = 100$ fs, slight deviations from the proper C_{3v} symmetry can be identified. They result from numerical errors due to the incomplete convergence of the SPF basis. These errors indicate that the maximum propagation time for which accurate wavefunction data can be obtained from the present calculations is reached at about $t = 100$ fs.

Summarizing, the movement of the wave packet in the coordinates that describe the location of the F atom with
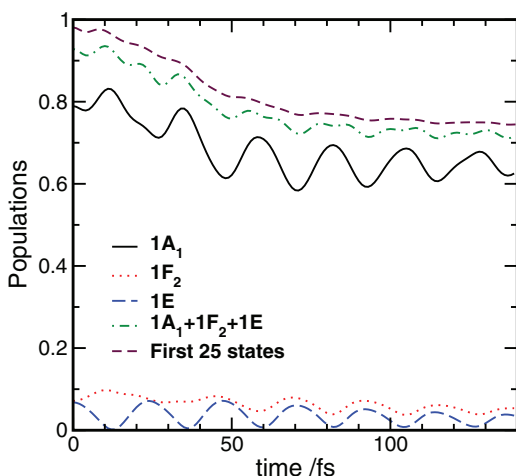
FIG. 5. Populations of the methane levels as a function of time.

FIG. 6. Absolute value of the autocorrelation function.

respect to the methane molecule is rather simple and predictable. A small fraction goes onto the product channel while the remaining part moves out in the reactant channel until it reaches the region of the van der Waals wells situated at $R > 3.30$ Å. At the same time, the wave packet spreads in all directions.

The internal vibrational dynamics of the CH_4 fragment was analysed by calculating the populations of the different methane states according to Eq. (13). Figure 5 shows the time evolution of these populations for the most prominent states, the vibrational ground state $1A_1$, and the bending excited states $1F_2$ and $1E$. Initially, the population of the ground state of CH_4 is almost 0.80, while the bending excited states $1F_2$ and $1E$ have populations nearly ten times smaller. Altogether the six lowest states corresponding to the $1A_1$, $1F_2$, and $1E$ levels amount to 93% of total population and the sum of the lowest 25 vibrational states (including additionally all double bending excited and single stretching excited levels) amounts to 98%. As the time goes on, the fraction of the wave packet that populates the lower vibrational states of methane decreases. This is not surprising since a non-negligibly part of the wave packet moves towards the products channels. We note, however, that this process is more rapid at the beginning of the propagation. Then, at about 80 fs, the curve showing the summed contribution of the first three levels ($1A_1$, $1F_2$, $1E$) tends to level out, as well as the curve corresponding to the first 25 states. This picture is coherent with the dynamics already analysed for the F atom coordinates. The wave packet is initially close to the transition state but it rapidly moves out from that region. Part of it goes to products and cannot be described by the vibrational states of methane. The other fraction moves towards the outer van der Waals wells and can be approximately described by the lowest three vibrational levels of methane. Finally we note that the curve showing the summed contributions of $1A_1$, $1F_2$, and $1E$ is rather smooth while the ones corresponding to the individual levels present significant oscillations. This indicates that the presence of the flourine atom induces a non-negligible coupling between the different vibrational states of methane and demonstrates
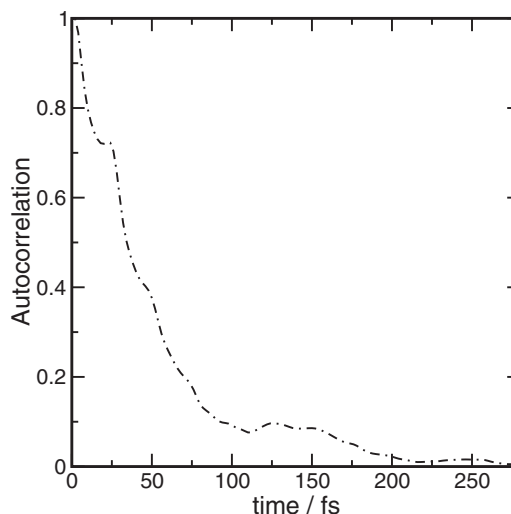
the limits of a simple model based on uncoupled methane eigenstates.

The autocorrelation function obtained by propagating the wavefunction for 140 fs is presented in Fig. 6. Since the calculation of the autocorrelation function at time t only requires the wavefunction at time $t/2$ (see Eq. (10)), the absolute value of the autocorrelation function for times up to 280 fs is displayed. It is a rather unstructured function with a nearly monotonic decrease. The only feature that stands out from this description is a small recurrence starting at ≈ 120 fs. For $t = 280$ fs the autocorrelation function has nearly vanished. Therefore, there is no need to introduce a damping function when computing the low-resolution spectrum. We should note, however, that recurrences could occur at later times as a consequence of slow motions such as the stretching vibration of the F-CH_4 complex. Since accurate wavefunction propagation for longer periods of time could not be achieved with the techniques and resources presently available, we cannot answer the question whether such recurrences appear on a longer time scale. If existing, these recurrences would give rise to fine structures superimposed on the low-resolution spectrum.

B. Convergence analysis

We have analysed the convergence of the computed spectra with respect to the size of the basis set and with respect to the propagation time. The result of such analysis is presented in this section. After many trials we found that basis set A_1 is a kind of minimal-size basis, appropriate to propagate the wave packet up to 100 fs. In this basis, the five degrees of freedom that depict the stretching vibrations and the asymmetric bending vibrations of the CH_3 fragment are treated at a Hartree level. Basis set A_2 is an improved version of basis set A_1, with more SPFs in the non-Hartree coordinates (θ, r, s, t, R, S, and T). One should note that these coordinates are the most important ones to describe the dissociation towards the $HF + CH_3$ channel as well as the spreading of the wave packet in the $F + CH_4$ channel. Basis set B_1 is also an improved version of
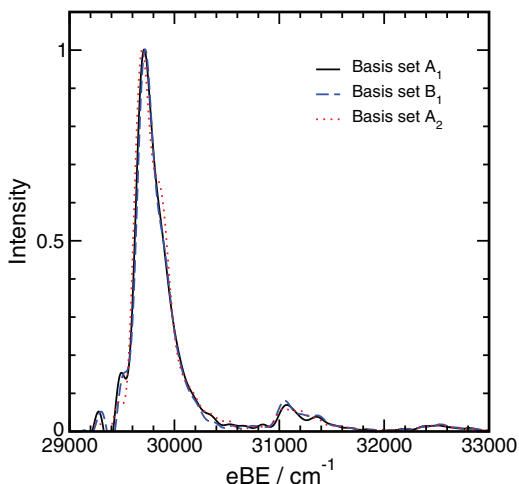
FIG. 7. Photodetachmet spectra computed with different basis sets.

FIG. 9. Comparison between the computed spectrum and the overall experimental spectrum of Ref. [86].

basis set A_1, but in this case the improvement is in the coordinates that describe the internal motions of the CH_3 fragment. Thus, basis set B_1 has the same number of SPFs in coordinates θ, r, s, t, R, S, and T as basis A_1, but treats no coordinate at a Hartree level. From the analysis of the natural populations of the SPFs in basis set B_1 we concluded that the Hartree treatment is appropriate for the stretching and the asymmetric bending vibrations of the CH_3 fragment. On the other hand, we found that the additional SPFs in the non-Hartree coordinates included in basis set A_2 get relatively high populations in the course of time. Therefore, we considered basis set A_2 to be the most accurate basis. It was used to run the longest propagations (140 fs) and the data presented above were based on this calculation. Figure 7 shows the photodetachment spectra computed with basis sets A_1, A_2, and B_1 for a propagation time of 100 fs. One finds that the differences between the basis sets discussed above have almost negligible effects on the computed spectra.

Figure 8 shows the spectra computed with basis set A_2 for propagation times equal to 80 fs, 100 fs, 120 fs, and 140 fs. Apart from the Fourier noise, which is larger for shorter
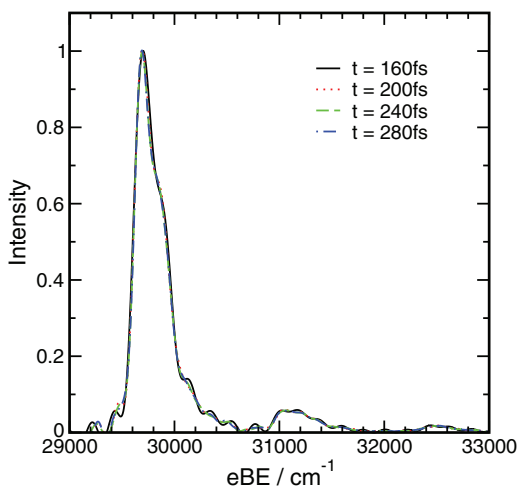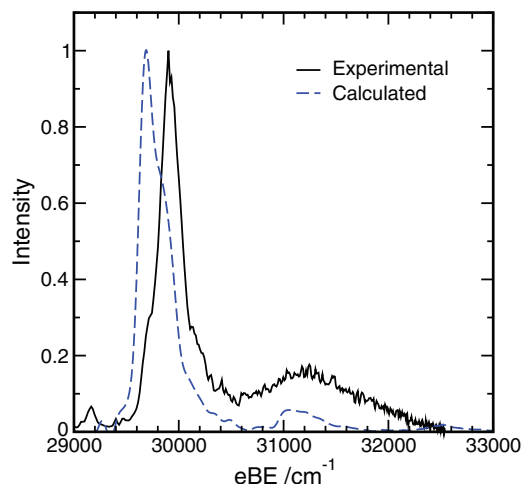
propagation times, all spectra look very much the same. There is a tiny shift in the position of the maximum, which is at 29703 cm^{-1} in the spectrum computed for 80 fs of propagation but is at 29691 cm^{-1} in the spectrum computed for 140 fs of propagation. Also, the shoulder of the main peak is slightly less pronounced in the spectrum corresponding to the shortest propagation time. However, these differences are tiny and even smaller than the differences resulting from the different basis sets (Fig. 7). Thus, one can conclude that the low-resolution spectrum is converged with respect to the propagation time employed. However, as discussed above, recurrences of a much larger time scale are not considered and, thus, eventually existing fine structure superimposed to the low-resolution spectrum presented is not resolved. Consequently, a description of the fine structure seen in recent high resolution spectra measured by Neumark and co-workers[86] is beyond the limits of the present study.

C. Comparison with experiments and interpretation

The spectrum computed with the best basis set (A_2) for the longest propagation time (140 fs) is presented in Fig. 9 along with the experimental low-resolution spectrum of Neumark and co-workers.[86] The maximum of the computed spectrum is at 29691 cm^{-1} and the full width of the peak at half maximum is 294 cm^{-1}. Besides, there is a significantly smaller, broad, and asymmetric peak shifted about 1400 cm^{-1} towards larger energies. The width, location, and shape of the main peak in the computed spectrum is similar to that of the experimental spectrum. However, there are differences in the detailed structure. The location of the maxima and relative position of the shoulders differ. The computed spectrum has a shoulder at $\approx 29\,841$ cm^{-1} close to the maximum height of the experimental spectrum (29 915 cm^{-1}), while the experimental spectrum has a shoulder at $\approx 29\,773$ cm^{-1} close the to the maximum height of the computed spectrum.

Differences between the computed and experimental spectrum are larger at the second peak, which is significantly higher and broader in the experiment. Besides, the

FIG. 8. Photodetachmet spectra computed with basis set A_2 for different times.

experimental spectrum shows a tiny peak on the left side of the main peak that is not present in the computed spectrum. Thus, while there is an overall satisfactory agreement between theory and experiment, with the main features of the experimental spectrum being also present in the computed spectrum, there are also noticeable discrepancies. This not surprising considering the complexity of the system under consideration and clearly indicates that further improvements are needed on the theoretical side.

The fact that the computed spectrum presents a second peak blue-shifted by about 1400 cm^{-1} compared to the main peak is somewhat striking. Previous studies assigned that peak to transitions to an excited electronic state of the neutral species,[86,87] but the present computations were performed on a single neutral surface. Clearly, a different explanation should apply to our results. In the search of that explanation the spectrum was decomposed into the contributions of different vibrational states of methane as described in Sec. II C.

The most important of such contributions are presented in Fig. 10. Panel (a) shows a comparison between the spectra computed in the usual way, i.e., applying Eq. (6), and the sum of the contributions of the three lowest vibrational levels of methane $\sigma_{1A_1}^{(0)}$, $\sigma_{1F_2}^{(0)}$, and $\sigma_{1E}^{(0)}$, obtained by applying Eq. (14) (please note that slight differences compared to the spectra presented above result from the fact that the "time doubling" of Eq. (10) could not be employed in this context). The comparison clearly shows that the three levels together nearly account for the whole computed spectrum. In order to identify the contributions of the different vibrational states of methane, they are plotted along with the summed contributions of the three levels: $\sigma_{1A_1}^{(0)}$ in panel (b) and $\sigma_{1F_2}^{(0)}$, $\sigma_{1E}^{(0)}$ in panel (c). Panel (b) shows that the main peak of the spectrum is almost exclusively due to the contribution of ground state methane while
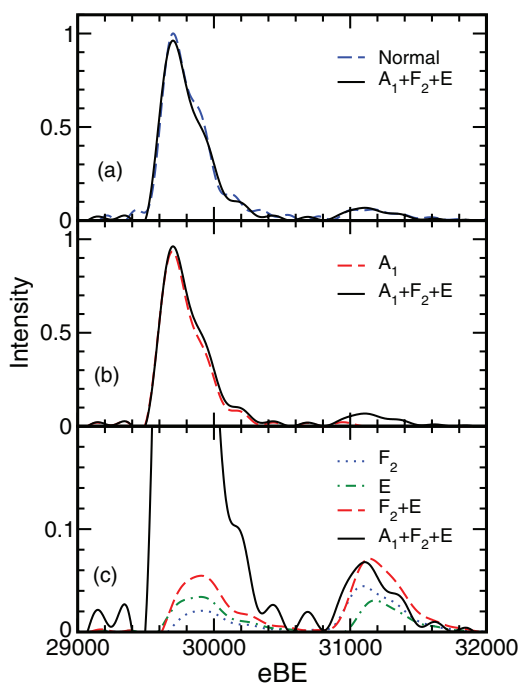
panel (c) indicates that the second peak is due to the summed contributions of levels 1F$_2$ and 1E. On top of this observation one should note that the energy difference between the main and the second peak of the spectrum is roughly equal to the vibrational excitation energy of the bending excited states of methane, 1F$_2$ and 1E (1300 cm^{-1} and 1522 cm^{-1}, respectively).

The following picture emerges from this analysis: the main peak of the spectrum is due to excitation to a state of the FCH$_4$ complex that mainly consists of ground state methane slightly perturbed by the presence of the F atom, while the second peak is due to excitation to FCH$_4$ states which consist of methane in the bending excited states 1F$_2$ and 1E. Since the perturbation exerted by the F atom is weak, the energy gap between the ground and the excited states of the complex is nearly the same than the one observed in isolated methane. Also, the presence of the F atom is responsible for the exchange of population between the ground and bending excited states observed in Fig. 5.

We want to stress that in no way the previous analysis rules out that excitation to an electronic excited state also contributes to the second peak in the experimental spectrum. Moreover, we note that the second peak is relatively higher and broader in the experimental spectrum than in the computed one. One could thus speculate that transitions to electronic excited states of the neutral species either provide additional intensity and "broadness" for the second peak or add an extended high-energy shoulder to the main peak which raises the baseline for the second peak. However, other explanations, such as limitations of the PESs employed in the present computations, could also be responsible for these differences. Clearly, quantum dynamics calculations which properly consider all three putative relevant potential energy surfaces of the F + CH$_4$ system are required to answer these questions reliably.

Neumark and co-workers also obtained the photodetachment spectrum for FCD$_4^-$ and found that the energy shift between the first and second peaks is, in this case, somewhat smaller than for FCH$_4^-$. Thus, the measured energy shift reduces from 1291 cm^{-1} to 1032 cm^{-1} upon deuteration,[86] which seems to be in line with the idea that the second peak has contributions of bending excited states of CH$_4$. However, the expected shift for FCD$_4^-$ ($\approx$913 cm^{-1}) is smaller than the observed value. Therefore, it is not clear if the observed difference in the position of the second peak is just due to the experimental uncertainty, as suggested in Ref. 86, or if there is a real mass effect on the vibrational energy levels. Hopefully, the computation of the photodetachment spectrum of FCD$_4^-$ could shed some light on this regard.

Differences between computations and experiments become larger if one compares with the experimental spectra of Ref. 87, which presents two peaks of similar width and high. However, significantly broader peaks are seen in experimental photodetachment spectrum of Ref. 87 compared to the one of Ref. 86. The additional spectra broadening seen in Ref. 87 presumably results from the specific experimental conditions. We believe that this fact can explain, at least partially, that our computations compare better with the experiments of Neumark *et al.*

FIG. 10. Contribution of different methane levels to the computed spectrum.

IV. CONCLUSIONS

Full-dimensional quantum dynamics simulations of the photodetachement spectrum of FCH_4^- employing the MCTDH approach have been presented and the dynamics of the system within the first 140 fs has been analysed in detail. It was found that the major part of the wave packet initially moves towards the $F + CH_4$ asymptote and later is located in the $F \cdot CH_4$ van der Waals region. Within the time period studied, only a minor part moves towards the $HF + CH_3$ asymptote. To assign the two peaks present in the photodetachment spectrum, a model which describes the FCH_4 system as a complex consisting of a methane molecule slightly perturbed by the presence of the F atom was successfully employed. The intense first peak results from FCH_4 complexes with CH_4 in its vibrational ground state $1A_1$ and the second much less intense peak corresponds to bending excited CH_4 in the $1F_2$ and $1E$ vibrational levels. The presence of the fluorine atom induces significant coupling between the vibrational levels of the methane fragment and therefore the vibrational populations oscillate in time.

Because of the limited propagation time, the energy resolution of the computed spectrum is in the range of a hundred cm^{-1}. While this allows for a comparison with the low-resolution experimental spectrum of Neumark and co-workers,[86] it is not sufficient to describe the fine structure present in the high resolution spectrum obtained by the same authors.

Qualitative agreement was found between the computed spectrum and the low-resolution experimental one obtained by Neumark and co-workers. However, a quantitative comparison showed differences in the detailed shape of the peaks and in the intensity ratio between the first and second peaks. The present quantum dynamics study has been limited to a single potential energy surface for the neutral system. It seems presently uncertain whether the two other electronic states correlating to the $F(^2P) + CH_4$ asymptote would have to be included in the computations to improve the comparison between theory and experiments, mainly at the second peak. On the other hand, clearly longer propagation times and a higher quality of the ground state neutral PES in the $F + CH_4$ channel are required to quantitatively reproduce and interpret the existing experimental data.

[1]W. Hu and G. C. Schatz, J. Chem. Phys. **125**, 132301 (2006).
[2]X. Yang, Annu. Rev. Phys. Chem. **58**, 433 (2007).
[3]D. C. Clary, Science **321**, 789 (2008).
[4]T.-S. Chu, K.-L. Han, M. Hankel, G. G. Balint-Kurti, A. Kuppermann, and R. Abrol, J. Chem. Phys. **130**, 144301 (2009).
[5]M. Qiu, Z. Ren, L. Che, D. Dai, S. A. Harich, X. Wang, X. Yang, C. Xu, D. Xie, M. Gustafsson et al., Science **311**, 1440 (2006).
[6]J. Aldegunde, J. M. Alvariño, M. P. de Miranda, V. S. Rábanos, and F. J. Aoiz, J. Chem. Phys. **125**, 133104 (2006).
[7]S.-H. Lee, F. Dong, and K. Liu, J. Chem. Phys. **125**, 133106 (2006).
[8]D. De Fazio, S. Cavalli, V. Aquilanti, A. A. Buchachenko, and T. V. Tscherbul, J. Phys Chem. A **111**, 12538 (2007).
[9]L. Che, Z. Ren, X. Wang, W. Dong, D. Dai, X. Wang, D. H. Zhang, X. Yang, L. Sheng, G. Li et al., Science **317**, 1061 (2007).
[10]Z. Ren, L. Che, M. Qiu, X. Wang, W. Dong, D. Dai, X. Wang, X. Yang, Z. Sun, B. Fu et al., PNAS **105**, 12662 (2008).
[11]F. Lique, M. H. Alexander, G. Li, H.-J. Werner, S. A. Nizkorodov, W. W. Harper, and D. J. Nesbitt, J. Chem. Phys. **128**, 084313 (2008).
[12]W. Dong, C. Xiao, T. Wang, D. Dai, X. Yang, and D. H. Zhang, Science **327**, 1501 (2010).
[13]F. Lique, G. Li, H.-J. Werner, and M. H. Alexander, J. Chem. Phys. **134**, 231101 (2011).
[14]C. Xiao, X. Xu, S. Liu, T. Wang, W. Dong, T. Yang, Z. Sun, D. Dai, X. Xu, D. H. Zhang et al., Science **333**, 440 (2011).
[15]S. Liu, X. Xu, and D. H. Zhang, J. Chem. Phys. **136**, 144302 (2012).
[16]J. Lin, J. Zhou, W. Shiu, and K. Liu, Science **300**, 966 (2003).
[17]J. Zhou, J. Lin, W. Shiu, S.-C. Pu, and K. Liu, J. Chem. Phys. **119**, 2538 (2003).
[18]J. Zhou, J. Lin, W. Shiu, and K. Liu, J. Chem. Phys. **119**, 4997 (2003).
[19]J. Zhou, J. Lin, and K. Liu, J. Chem. Phys. **119**, 8289 (2003).
[20]J. Zhou, W. Shiu, J. Lin, and K. Liu, J. Chem. Phys. **120**, 5863 (2004).
[21]W. Shiu, J. Lin, and K. Liu, Phys. Rev. Lett. **92**, 103201 (2004).
[22]J. Zhou, J. Lin, and K. Liu, J. Chem. Phys. **121**, 813 (2004).
[23]J. Zhou, W. Shiu, J. Lin, and K. Liu, J. Chem. Phys. **124**, 104309 (2006).
[24]J. Zhou, J. Lin, W. Shiu, and K. Liu, Phys. Chem. Chem. Phys. **8**, 3000 (2006).
[25]B. Zhang, S. Yan, and K. Liu, J. Phys. Chem. A **111**, 9263 (2007).
[26]W. Zhang, H. Kawamata, and K. Liu, Science **325**, 303 (2009).
[27]G. Czakó, Q. Shuai, K. Liu, and J. M. Bowman, J. Chem. Phys. **133**, 131101 (2010).
[28]W. W. Harper, S. A. Nizkorodov, and D. J. Nesbitt, J. Chem. Phys. **113**, 3670 (2000).
[29]W. Shiu, J. J. Lin, K. Liu, M. Wu, and D. H. Parker, J. Chem. Phys. **120**, 117 (2004).
[30]H. Kawamata, W. Zhang, and K. Liu, "Imaging effects of the antisymmetric stretch excitation of CH_4 in the reaction with the F atom," Faraday Discuss. (in press).
[31]Z. H. Kim, H. A. Bechtel, and R. N. Zare, J. Am. Chem. Soc. **123**, 12714 (2001).
[32]Z. H. Kim, H. A. Bechtel, and R. N. Zare, J. Chem. Phys. **117**, 3232 (2002).
[33]H. A. Bechtel, Z. H. Kim, J. P. Camden, and R. N. Zare, J. Chem. Phys. **120**, 791 (2004).
[34]H. A. Bechtel, J. P. Camden, D. J. A. Brown, and R. N. Zare, J. Chem. Phys. **120**, 5096 (2004).
[35]Z. H. Kim, H. A. Bechtel, J. P. Camden, and R. N. Zare, J. Chem. Phys. **122**, 084303 (2005).
[36]S. Yoon, S. Henton, A. N. Zivkovic, and F. F. Crim, J. Chem. Phys. **116**, 10744 (2002).
[37]S. Yoon, R. J. Holiday, E. L. Sibert III, and F. F. Crim, J. Chem. Phys. **119**, 9568 (2003).
[38]B. Retail, J. K. Pearce, C. Murray, and A. J. Orr-Ewing, J. Chem. Phys. **122**, 101101 (2005).
[39]B. Zhang and K. Liu, J. Chem. Phys. **122**, 101102 (2005).
[40]J. Zhou, J. J. Lin, B. Zhang, and K. Liu, J. Phys. Chem. A **108**, 7832 (2004).
[41]M. J. Bass, M. Brouard, R. Ciresasa, A. P. Clark, and C. Vallance, J. Chem. Phys. **123**, 094301 (2005).
[42]R. J. Holiday, C. H. Kwon, C. J. Annesly, and F. F. Crim, J. Chem. Phys. **125**, 133101 (2006).
[43]M. R. Martin, D. J. A. Brown, A. S. Chiou, and R. N. Zare, J. Chem. Phys. **126**, 044315 (2006).
[44]S. Yan, Y.-T. Wu, B. Zhang, X.-F. Yue, and K. Liu, Science **316**, 1723 (2007).
[45]Y.-T. Wu and K. Liu, J. Chem. Phys. **129**, 154302 (2008).
[46]H. Kawamata, S. Tauro, and K. Liu, Phys. Chem. Chem. Phys. **10**, 4378 (2008).

[47]S. Yan, Y.-T. Wu, B. Zhang, X.-F. Yue, and K. Liu, PNAS **105**, 12667 (2008).

[48]T. Takayanagi, J. Chem. Phys. **104**, 2237 (1996).

[49]H.-G. Yu and G. Nyman, J. Chem. Phys. **111**, 3508 (1999).

[50]M. Wang, Y. Li, J. Zhang, and D. Zhang, J. Chem. Phys. **113**, 1802 (2000).

[51]F. Huarte-Larrañaga and U. Manthe, J. Chem. Phys. **113**, 5115 (2000).

[52]D. Wang and J. M. Bowman, J. Chem. Phys. **115**, 2055 (2001).

[53]M. Yang, D. H. Zhang, and S.-Y. Lee, J. Chem. Phys. **117**, 9539 (2002).

[54]T. Wu, H.-J. Werner, and U. Manthe, Science **306**, 2227 (2004).

[55]R. van Harrevelt, G. Nyman, and U. Manthe, J. Chem. Phys. **126**, 084303 (2007).

[56]G. Nyman, R. van Harrevelt, and U. Manthe, J. Phys. Chem. A **111**, 10331 (2007).

[57]Z. Xie, J. M. Bowman, and X. Zhang, J. Chem. Phys. **125**, 133120 (2006).

[58]G. Schiffel and U. Manthe, J. Chem. Phys. **132**, 191101 (2010).

[59]G. Schiffel and U. Manthe, J. Chem. Phys. **133**, 174124 (2010).

[60]Y. Zhou, B. Fu, C. Wang, M. A. Collins, and D. H. Zhang, J. Chem. Phys. **134**, 064323 (2011).

[61]Y. Zhou, C. Wang, and D. H. Zhang, J. Chem. Phys. **135**, 024313 (2011).

[62]W. Zhang, Y. Zhou, G. Wu, Y. Lu, H. Pan, B. Fu, Q. Shuai, L. Liu, S. Liu, L. Zhang *et al.*, PNAS **107**, 12782 (2010).

[63]R. T. Skodje, D. Skouteris, D. E. Manolopoulos, S.-H. Lee, F. Dong, and K. Liu, J. Chem. Phys. **112**, 4536 (2000).

[64]D. Troya, I. Millán, I. Baños, and M. González, J. Chem. Phys. **120**, 5181 (2004).

[65]G. Czakó, B. C. Shepler, B. J. Braams, and J. M. Bowman, J. Chem. Phys. **130**, 084301 (2009).

[66]J. F. Castillo, F. J. Aoiz, L. Bañares, E. Martinez-Nuñez, A. Fernández-Ramos, and S. Vazquez, J. Phys. Chem. A **109**, 8459 (2005).

[67]D. Troya, J. Chem. Phys. **123**, 214305 (2005).

[68]J. Espinosa-García, J. L. Bravo, and C. Rángel, J. Phys. Chem. A **111**, 2761 (2007).

[69]J. P. Layfield, A. F. Sweeney, and D. Troya, J. Phys. Chem. A **113**, 4294 (2009).

[70]G. Czakó and J. M. Bowman, J. Am. Chem. Soc. **131**, 17534 (2009).

[71]G. Czakó and J. M. Bowman, J. Chem. Phys. **131**, 244302 (2009).

[72]X. Tian, T. Gao, N. He, and Z. Zhang, Mol. Phys. **106**, 2717 (2008).

[73]J. Espinosa-García and J. L. Bravo, J. Phys. Chem. A **112**, 6059 (2008).

[74]J. Espinosa-García, J. Phys. Chem. A **111**, 3497 (2007).

[75]J. Espinosa-García, Chem. Phys. Lett. **488**, 153 (2010).

[76]C. Rángel, M. Navarrete, and J. Espinosa-García, J. Phys. Chem. A **109**, 1441 (2005).

[77]O. Roberto-Neto, F. B. Machado, and F. R. Ornellas, Chem. Phys. **315**, 27 (2005).

[78]T. Chu, K. Han, and J. Espinosa-García, J. Chem. Phys. **131**, 244303 (2009).

[79]G. Nyman and J. Espinosa-García, J. Phys. Chem. A **111**, 11943 (2007).

[80]D. M. Neumark, Phys. Chem. Chem. Phys. **7**, 433 (2005).

[81]D. M. Neumark, J. Phys. Chem. A **112**, 13287 (2008).

[82]P. G. Wenthold, D. A. Hrovat, W. T. Borden, and W. C. Lineberger, Science **272**, 1456 (1996).

[83]A. Weaver and D. M. Neumark, Faraday Discuss. **91**, 5 (1991).

[84]S. E. Bradforth, D. W. Arnold, D. M. Neumark, and D. E. Manolopoulos, J. Chem. Phys. **99**, 6345 (1993).

[85]C. L. Russell and D. E. Manolopoulos, Chem. Phys. Lett. **256**, 465 (1996).

[86]T. I. Yacovitch, E. Garand, J. B. Kim, C. Hock, T. Theis, and D. M. Neumark, "Vibrationally resolved transition state spectroscopy of the F+H$_2$ and F+CH$_4$ reactions," Faraday Discuss. (in press).

[87]M. Cheng, Y. Feng, Y. Du, Q. Zhu, W. Zheng, G. Czakó, and J. M. Bowman, J. Chem. Phys. **134**, 191102 (2011).

[88]H.-D. Meyer, U. Manthe, and L. S. Cederbaum, Chem. Phys. Lett. **165**, 73 (1990).

[89]U. Manthe, H.-D. Meyer, and L. S. Cederbaum, J. Chem. Phys. **97**, 3199 (1992).

[90]F. Huarte-Larrañaga and U. Manthe, J. Phys. Chem. A **105**, 2522 (2001).

[91]F. Huarte-Larrañaga and U. Manthe, J. Chem. Phys. **116**, 2863 (2002).

[92]F. Huarte-Larrañaga and U. Manthe, J. Chem. Phys. **117**, 4635 (2002).

[93]T. Wu, H.-J. Werner, and U. Manthe, J. Chem. Phys. **124**, 164307 (2006).

[94]S. Andersson, G. Nyman, A. Arnaldsson, U. Manthe, and H. Jónsson, J. Phys. Chem. A **113**, 4468 (2009).

[95]G. Schiffel, U. Manthe, and G. Nyman, J. Phys. Chem. A **114**, 9617 (2010).

[96]G. Schiffel and U. Manthe, J. Chem. Phys. **132**, 084103 (2010).

[97]U. Manthe, Chem. Phys. Lett. **241**, 497 (1995).

[98]D. H. Zhang and J. C. Light, J. Chem. Phys. **104**, 6184 (1996).

[99]F. Huarte-Larrañaga and U. Manthe, J. Chem. Phys. **123**, 204114 (2005).

[100]G. Czakó, B. J. Braams, and J. M. Bowman, J. Phys. Chem. A **112**, 7466 (2008).

[101]C. Evenhuis, G. Nyman, and U. Manthe, J. Chem. Phys. **127**, 144302 (2007).

[102]D. O. Harris, G. G. Engerholm, and W. D. Gwinn, J. Chem. Phys. **43**, 1515 (1965).

[103]A. S. Dickinson and P. R. Certain, J. Chem. Phys. **49**, 4209 (1968).

[104]J. C. Light, I. P. Hamilton, and J. V. Lill, J. Chem. Phys. **82**, 1400 (1985).

[105]D. Kosloff and R. Kosloff, J. Comp. Phys. **52**, 35 (1983).

[106]U. Manthe, J. Chem. Phys. **105**, 6989 (1996).

[107]M. H. Beck and H.-D. Meyer, Z. Phys. D **42**, 113 (1997).

[108]U. Manthe, Chem. Phys. **329**, 168 (2006).

[109]R. Wodraszka, J. Palma, and U. Manthe, "Vibrational dynamics of the C$_4$F$^-$ complex," J. Phys. Chem. A (in press).

[110]U. Manthe, J. Chem. Phys. **128**, 064108 (2008).